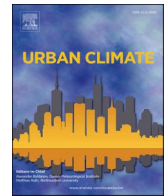




ELSEVIER

Contents lists available at [ScienceDirect](https://www.sciencedirect.com)

Urban Climate

journal homepage: www.elsevier.com/locate/uclim

Identifying the effect of monsoon floods on vegetation and land surface temperature by using Google Earth Engine

Sk Nafiz Rahaman^{*}, Nishat Shermin

Urban and Rural Planning Discipline, Khulna University, Khulna 9208, Bangladesh

ARTICLE INFO

Keywords:

Flood mapping
Vegetation
LST
Google Earth Engine
Satellite imagery

ABSTRACT

Flood is one of the most devastating climatic disasters around the world. The physical and infrastructural damage of floods is uncontrollable and challenging to recover. Though the mismanagement of the water system is one cause of flood, some countries face a seasonal natural flood, which is impossible to avoid. The history of flood affection in these countries are long, and people don't have any other choice but to adapt to this circumstance every year. The continuous flood event has several climatic impacts that are not broadly documented and remain in the shadows of severe infrastructural damage. This research aims to identify the effect of monsoon floods on vegetation and land surface temperature (LST). The study area is the northeast part of Bangladesh, a highly flood-prone area. The research incorporates Google Earth Engine (GEE) to manage the satellite image data related to this research which are Sentinel-1 SAR imagery and Landsat-8 imagery. Six years of data from 2015 to 2020 have been taken to continuously monitor the flooded area, vegetation, and LST dynamics. Primary results indicate a yearly increase and decrease of the flooded area with 57.3% highest increase rate in 2019. A continuous increase of Enhanced Vegetation Index (EVI) value and decrease of LST has a changing pattern similarity with flooded area fluctuation over the year. Also, the flooded areas have around 50% less mean EVI value than the non-flooded areas, eventually rising average LST in flooded areas. 10,024 grids of 1 km × 1 km have been used to extensively analyze the relationship of flood and EVI through correlation and linear regression. The final result reveals a clear negative correlation value (less than 0.56 for all the years) of EVI with flooded areas, having the highest R-squared value of 0.4325 in 2017.

1. Introduction

Numerous disasters over the last few decades have shown a significant rise in the likelihood of water-related events occurring everywhere on the planet. Tsunamis, storm surges, river floods, flash floods, mass migration, and droughts are all examples of such phenomena. The primary drivers of this risk are the global population's continued growth; the concentration of people in high-risk areas such as coastlines, floodplains, and hillsides; an increase in the vulnerability of assets, infrastructure, and social systems; and the effects of climate and environmental change (Kron, 2015).

Each year, large and destructive floods occur. Heavy floods devastated Pakistan, India, and China in the summer of 2010, Colombia in October to December 2010, and Australia in the southern summer of 2010/11. In 2010, China witnessed the largest estimated

^{*} Corresponding author.

E-mail address: nafizrahaman1@gmail.com (S.N. Rahaman).

annual flood damage in the country's history, with a reported total loss of US\$51 billion. In 2010, about 2000 people died directly as a result of monsoon floods in Pakistan. Severe flooding occurred in Africa, Mozambique, Namibia, South Africa, and Uganda; in the Americas, Brazil, Columbia, Mexico, and the United States; and in Asia, Cambodia, China, India, the Koreans, Pakistan, the Philippines, and Thailand, with each disaster claiming at least 50 lives (over 1000 in Colombia and the Philippines). In 2012, "killer floods" killed over 50 people in Madagascar, Niger, and Nigeria; Bangladesh, China, India, North and South Korea, the Philippines, and Russia in Asia; and Argentina, the United States of America, and Haiti in the Americas (Kundzewicz et al., 2005, 2014; Taye et al., 2011).

Nearly a billion people are estimated to live in flood-prone areas by 2050, a figure that is forecast to triple due to erratic precipitation and rapid population growth. Flooding claimed 6.8 million lives globally throughout the twentieth century. According to recent study, the floods affected 2.3 billion people, making them the biggest natural disaster between 1995 and 2015. Inundation frequency and severity are increasing at an alarming rate in the context of climate change, with a conspicuous fourfold increase throughout Asia between 1982 and 2006. Floods' spatial extent and regularity provide an advantage for government and disaster relief agencies, which are obliged to respond swiftly and effectively to flood-affected persons. By identifying high-risk areas, the destructive impacts of floods on people and agriculture may be mitigated (Doocy et al., 2013; IIRRI, 2019; UNU, 2019).

The Ganges, Brahmaputra, Meghna (GBM) basins of Bangladesh are among the world's most flood-prone basins. As part of these large reservoirs and much of the region less than 7 m above average sea level, Bangladesh is affected by the cumulative impacts of flooding owing to hill-sloping water, the buildup of water from upstream catchments and the locally high precipitation caused by drainage congestion. The nation has a lengthy history of catastrophic floods that badly affected lives and property (Banerjee, 2010; Biswas, 2008; Chowdhury and Moore, 2017; Dasgupta et al., 2011; Rasid and Pramanik, 1993). Around 20,000 fatalities were recorded as a result of floods between 1954 and 2007. The Bangladesh Bureau of Statistics study revealed that 56.62% of households were impacted by disasters at least once in 2009–2014. Of them, 24.44% were impacted by flood occurrences. More than 80% of the country is prone to flooding. In an ordinary year, around 20–25% of the country's territory is flooded, but in severe years, the flooded territory constitutes more than 60% of the country. More than 30% of the country's regions were flooded during the 2017 storm, resulting in at least 134 fatalities and over 5.7 million people (Islam, 2016; Kundzewicz et al., 2014; Lin et al., 2019; Mirza, 2011; Monirul Qader Mirza, 2002). It is the fourth most prominent nation in the world to produce rice. Ever since local rice production is hindered by climate-induced natural disasters, including floods, droughts and cyclones, food security is still a problem for this country. In Bangladesh, flooding is the most frequent and has a significant impact on rice output. Identifying regularly inundated regions and flooded vegetation areas is thus essential to mitigate flood occurrences, reduce property damage, and ensure Bangladesh's food security (Singha et al., 2020).

Flood dynamics, frequency and scope maps are important in the planning and developing regional policies for flood mitigation, adaptation and infrastructure for flood protection. The fast monitoring of flood conditions, including mapping floods and damage, is crucial for an efficient response during flood occurrences. Flood forecasting and flood modelling are essential for risk reduction before any flood occurrence (Singha et al., 2020; Uddin et al., 2019). Currently, the Flood Forecasting and Warning Center (FFWC) produces early alert and monitoring information when water levels fluctuate in the central river systems in Bangladesh. The degree of flooding is also determined by comparing the amount of water with the national Digital Elevation Model (DEM). To generate flood maps using hydrological models, an up-to-date and accurate DEM and computer system is necessary to simulate the impacts of barriers on the floodplains (Ahmad and Ahmed, 2003; Amarnath and Rajah, 2016; Jung et al., 2014; Shen et al., 2019). Unfortunately, there are frequently inadequate precise DEM and infrastructure data (Uddin et al., 2019). Flood management is not successful for the timely monitoring of flood occurrences based on water level predictions to provide a geographically dispersed flood region. The fluvial gauge data and model simulation can forecast fluctuation on the national scale, but the precise geographical extent of the flooded regions cannot be provided. In contrast to the water level flood map, the satellite flood maps offer geographical distribution and extent of floods over time and at close-real time in different spatial resolutions and can often monitor high efficiency and accuracy in flooded areas. Surveys in fields in flooded regions are difficult and impossible for broad areas, while satellite monitoring is a viable option in the near-real monitoring of floods (Huang et al., 2014; Singha et al., 2020).

In order to monitor flooded regions, two kinds of satellite observations are available: optical imaging and Synthetic Aperture Radar (SAR). To derive flood maps, data from several optical sensors, such as the Moderate Resolution Imaging Spectroradiometer (MODIS), Advanced Very High Resolution Radiometer (AVHRR) and Landsat, were utilized (Qi et al., 2009; Sheng et al., 2001). However, passive optical sensors that rely on sun reflection and overcast days cannot capture the planet's surface. The active SAR sensor can gather data from the cloud deck and is particularly useful for flood surveillance in regions with cloud cover and a wet mountain season. Flooded regions produce a low back dispersion signal, and water surfaces seem to be highly black in SAR pictures, making them distinct from other types of land covering areas, such as vegetation, land for agriculture, bare land, or built-up areas. In the course of a major flood, for example, the momentary roughness of the surface of the water caused by wind or severe rainfall may challenge the detection of certain flooded regions (Clement et al., 2018; Long et al., 2014; Matgen et al., 2011; Notti et al., 2018). The radar shadow in the SAR pictures is black and maybe misclassified as flooded water, and two backscatter signals and radar shadows from high-density urban structures hinder the detection (Brisco et al., 2009; Mason et al., 2010). Nonetheless, the capacity of SAR to gather data through thick cloud formations and the abundance of Sentinel-1 data make SAR a vital instrument to map and monitor flooding during the rainy season (Singha et al., 2020).

There have been many suggested SAR-based flood detection approaches, which mainly utilize one or more methodologies. Histogram thresholding or clustering, fuzzy grading, area of growth, and texture analysis are some of the examples (Martinis et al., 2009, 2015, 2018; Pradhan et al., 2014; Senthilnath et al., 2013; Tsyganskaya et al., 2018; Twele et al., 2016). Most of these methods utilize a single date picture to identify flood occurrences. A time series of pictures is used for multi-temporal change detection techniques to identify pre- and post-flood land cover (Li et al., 2018; Long et al., 2014). The picture of the land cover is coupled with additional

methods, such as histogram threshold or image segmentation, to recognize flooded regions. This technique gives more precision compared with a single picture-based method. Some techniques utilize high-resolution flood detection maps. In low-lying areas such as Bangladesh, however, elevation maps are not useful. In the past, optical imagery (Landsat 8) and SAR (COSMO-SkyMed) were used to map floods using vector machine classification devices in China (Clement et al., 2018; Manfreda et al., 2011; Sanders, 2007; Tong et al., 2018). A mixed process was used to map floods using Sentinel-1 SAR data to combine texture analysis with a fugitive categorization

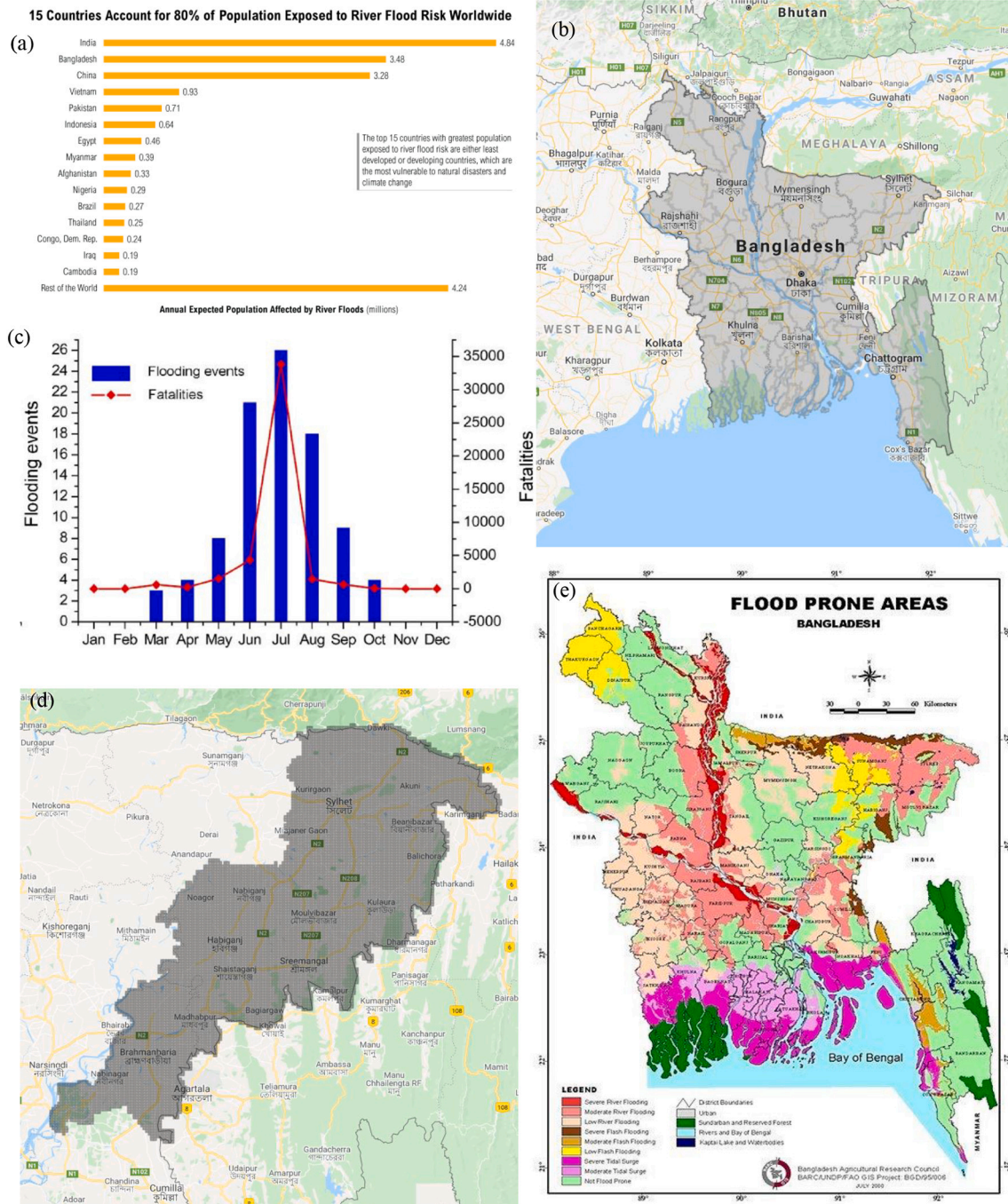


Fig. 1. Study area of the research; (a) 15 countries where around 80% of population is exposed to flood (Source: World Resource Institute); (b) Area of Bangladesh; (c) total number of flood events and fatalities between 1960 and 2018 in Bangladesh (Source: EM-DAT, The International Disaster Database); (d) Area of analysis (4 Districts and 32 Cities and Upazilas of Bangladesh); (e) Flood prone areas of Bangladesh (Source: Bangladesh Agricultural Research Council (BARC)/GIS Project, BGD/95/006).

system and a change detection technique. The probability-based method to map floods using SAR imagery has been developed recently. Data from the crowd were also coupled with satellite data, and geo-statistical analyzes were utilized to generate flood maps (Amitrano et al., 2018; Hostache et al., 2018; Panteras and Cervone, 2018).

In this paper, the main objective is to identify the effect of floods on vegetation and land surface temperature. The GEE cloud computing platform has been used for this purpose. The use of GEE is still very new in flood mapping and more efficient than conventional software-based techniques (Singha et al., 2019, 2020). It allows managing and analyzing large sets of data simultaneously, which is essential for big data-based research. The research answers a major question: how much yearly flooded area fluctuation impacts the overall vegetation and LST condition? Limited works have been done on this topic, and most of them show the flood effect on crops and agricultural lands. Incorporating the overall vegetation and LST is the uniqueness of this research.

2. Methods

2.1. Study area

The study area of this research is the northeast region of Bangladesh (Fig. 1d). The country is located in South Asia and is one of the world's most prone to floods (Fig. 1a). It spans around 147,000 km² of land and stretches between 20°44'00" to 26°37'51"N of latitude and 88°0'14" to 92°40'08"E of longitude (Fig. 1b). Bangladesh's overall population is about 163 million. The terrain of Bangladesh is flat in the southeast, with an average altitude of over 300 m, except the Chittagong Hill Tracts (CHT) areas. The Ganges, Brahmaputra and Meghna are the three main rivers that run through Bangladesh, with 230 minor rivers. The nation has a subtropical monsoon climate with an average yearly temperature of 18 °C to 29 °C (Singha et al., 2020).

In recent years, continuous rainfall in Bangladesh has created floods. The EM-DAT database revealed an unequal temporary distribution between 1960 and 2018 of 94 flood occurrences, although the trend in flood frequencies was usually growing. Floods between May and October were particularly frequent with heavy monsoon rain (Fig. 1c). A total of 52,616 individuals were reported to have perished from flooding between 1960 and 2018, mainly between May and October. Apart from the deaths, flooding in Bangladesh has destroyed countless homes, infrastructure and agriculture. Flooding occurrences are anticipated to rise in the next decades as the climate changes.

The northeast part of Bangladesh has been selected for the study area, including 4 Districts (Brahmanbaria, Hobiganj, Moulvibazar and Sylhet) with 32 Upazilas/City Corporation. This region has continuous flash flooding and moderate level river flooding areas (Fig. 1e). Also, there is a large area of vegetation with agricultural lands, making it suitable for studying the relationship between flood and vegetation.

2.2. Data

2.2.1. Data for flood detection

Sentinel-1 SAR GRD: C-band Synthetic Aperture Radar Ground Range Detected, log scaling imagery of European Space Agency (ESA) has been used to detect and identify the flooded areas. The Sentinel-1 mission contains data from a C-Band Synthetic Aperture Radar (SAR) dual-polarization sensor. This collection contains the S1 Ground Range Detected (GRD) scenes, processed using the Sentinel-1 toolbox in order to produce a calibrated, ortho-corrected output. This collection includes all scenes from the GRD. Each scene includes one of 3 (10, 25 or 40 m) resolutions, 4 band combinations (relative to the scene polarization) and 3 instrument modes. The use of the collection in a mosaic setting is probably need a homogenous set of bands and parameters to filter. Each scene includes either 1 or 2 of 4 potential polarization bands, based on the polarization settings of the instrument. Possible combinations include VV or HH single bands and VV + VH and HH + HV dual bands:

1. VV: single co-polarization, vertical transmit/vertical receive
2. HH: single co-polarization, horizontal transmit/horizontal receive
3. VV + VH: dual-band cross-polarization, vertical transmit/horizontal receive
4. HH + HV: dual-band cross-polarization, horizontal transmit/vertical receive

Each picture additionally has an extra "angle" band with the estimated ellipsoid incidence angle in degrees at each location. This band is produced by interpolating the 'incidenceAngle' attribute of the grid field 'geolocationGridPoint' that comes with each asset.

Each scene was pre-processed with Sentinel-1 Toolbox using the following steps:

1. Thermal noise removal
2. Radiometric calibration
3. Terrain correction using SRTM 30 or ASTER DEM for areas greater than 60 degrees latitude, where SRTM is unavailable. The final terrain-corrected values are converted to decibels via log scaling ($10 \cdot \log_{10}(x)$). (ESA, E.S.A., 2019).

Besides Sentinel-1 SAR collection, two other products have been used to identify the flooded area. One is the WWF HydroSHEDS Void-Filled DEM, 3 Arc-Seconds from which the DEM has been collected. HydroSHEDS is a mapping product that offers hydrographic information in a uniform manner for regional and worldwide applications. It provides a series of geo-referenced data sets (vector and raster) at different levels, including river networks, water shift borders, drainage routes and accumulations of flow. HydroSHEDS

(SRTM) is based on elevation data from the NASA Shuttle Radar Topography Mission in 2000 (ESA, E.S.A, 2020).

Another one is the JRC Global Surface Water Mapping Layers, v1.3, for identifying the permanent waterbodies. This dataset includes maps of the location and the temporary distribution of surface waters between 1984 and 2020 and information on their extent and evolution (GEE, 2020).

2.2.2. Data for NDVI, EVI and LST calculation

NDVI, EVI and LST have been calculated from USGS Landsat 8 Collection 1 Tier 1 and Real-Time data Raw Scenes. All the images that are used have less than 5% cloud coverage. Landsat scenes of the greatest data quality available are positioned in Tier 1 and are deemed appropriate for studying time series. Tier 1 contains data processed by Level-1 Precision Terrain (L1TP), which has well-known radiometry and is intercalibrated in various Landsat sensors. Tier 1 sceneries are consistent in their geo-registration and within specified limits [≤ 12 -m root mean square error (RMSE)]. All Tier 1 Landsat data may be deemed consistent and intercalibrated across the whole collection (independent of the sensor) (Google Earth Engine, 2021).

2.3. Flooded area extraction

The entire process of flooded area extraction has been done through Google Earth Engine (GEE) (Gandhi, 2020). Algorithm 1 is showing the developed code in GEE code editor. The first part of the process is to select image data when the flood event occurs. Besides this, another image data is needed before the flooding event. The most affected time of the year is June to August (Fig. 1c). For this research, July and August data has been taken for six years (2015–2020). The before flooding event data has been selected from January and February as these are the two driest months in Bangladesh (Fig. 1c).

The Interferometric Wide (IW) swath mode of Sentinel-1 SAR is the primary land acquisition method and meets the bulk of service needs. It receives data with a spatial resolution of 250 km at 5 m and 20 m (single look). IW mode collects 3 sub-swaths utilizing Terrain Observation with Progressive Scans SAR (TOPSAR). In addition to the range of beams as used in ScanSAR, the TOPSAR technology additionally guides the beam electronically from rear to rear in the azimuth direction for each burst, preventing scalloping and resulting in homogenous picture quality across the swath (De Zan and Guarnieri, 2006; ESA, 2021). The DESCENDING orbit properties have been used (Algorithm 1, Line 5–11).

The bands that have been used for flood detection is the VV and VH. The ratio of VV and VH is the RGB composite of the image. This is a way to understand whether the image set has been selected correctly. The RefinedLee function has been used to smoothen the image and increase the quality of the analysis (ESA, 2021). After that, the after flooded image has been divided by the before flooded image. This creates an image of the difference between the before flood and the after flood. After trying several values, a threshold value of 1.25 has been taken as the flooded regions as this value creates a reasonable amount of flooded area. That means values that are more than 1.25 is the flooded regions (Algorithm 1, Line 19–20).

JRC Global Surface Water Mapping Layers, v1.3 dataset has been used to identify the permanent and semipermanent waterbodies of the study area. The 'seasonality' band of this dataset has values from 0 to 12. 0 means there is no water at any time of the year, where 12 means water throughout the whole year. In this case, value 5 has been used, which means that places with waters for 5 months of the year have been detected as permanent or semipermanent waterbodies (Algorithm 1, Line 21–25).

WWF HydroSHEDS Void-Filled DEM, 3 Arc-Seconds has been used to remove the steeper areas where the flood cannot be affected. The value ranged from -424 to 8642 m. Regions that are more than 5 m high has been selected as flood unaffected areas (Algorithm 1, Line 26–35).

Algorithm 1. Flooded area extraction

```

1 var beforeStart = '2019-01-15';
2 var beforeEnd = '2019-02-10';
3 var afterStart = '2019-03-01';
4 var afterEnd = '2019-06-30';
5 var collection = ee.ImageCollection('COPERNICUS/S1_GRD')
6 .filter(ee.Filter.eq('instrumentMode', 'IW'))
7 .filter(ee.Filter.listContains('transmitterReceiverPolarisation', 'VH'))
8 .filter(ee.Filter.eq('orbitProperties_pass', 'DESCENDING'))
9 .filter(ee.Filter.eq('resolution_meters', 10))
10 .filterBounds(geometry)
11 .select('VH');
12 var beforeCollection = collection.filterDate(beforeStart, beforeEnd)
13 var afterCollection = collection.filterDate(afterStart, afterEnd)
14 var before = beforeCollection.mosaic().clip(geometry);
15 var after = afterCollection.mosaic().clip(geometry);
16 var beforeFiltered = ee.Image(toDB(RefinedLee(toNatural(before))));
17 var afterFiltered = ee.Image(toDB(RefinedLee(toNatural(after))));
18 var difference = afterFiltered.divide(beforeFiltered);
19 // Define a threshold

```

```

20 var diffThreshold = 1.25;
21 // Initial estimate of flooded pixels
22 var flooded = difference.gt(diffThreshold).rename('water').selfMask();
23 // Mask out area with permanent/semi-permanent water
24 var permanentWater = gsw.select('seasonality').gte(5).clip(geometry);
25 var flooded = flooded.where(permanentWater, 0).selfMask();
26 // Mask out areas with more than 5 percent slope using the HydroSHEDS DEM
27 var slopeThreshold = 5;
28 var terrain = ee.Algorithms.Terrain(hydrosheds);
29 var slope = terrain.select('slope');
30 var flooded = flooded.updateMask(slope.lt(slopeThreshold));
31 // Remove isolated pixels
32 // connectedPixelCount is Zoom dependent, so visual result will vary
33 var connectedPixelThreshold = 8;
34 var connections = flooded.connectedPixelCount(25);
35 var flooded = flooded.updateMask(connections.gt(connectedPixelThreshold));
36 // Calculate Affected Area
37 var stats = flooded.multiply(ee.Image.pixelArea()).reduceRegion({
38   reducer: ee.Reducer.sum(),
39   geometry: geometry,
40   scale: 30,
41   maxPixels: 1e10,
42   tileScale: 16
43 });

```

2.4. Calculating vegetation

2.4.1. Normalized difference vegetation index

Normalized difference vegetation index (NDVI) is one of the most common theoretical and practical practices to understand vegetation levels from remote sensing data. Its value range is -1 to 1 , indicating a high possibility of vegetation area when the value is close to 1 . For USGS Landsat 8 Collection 1 Tier 1 and Real-Time data Raw Scenes, the Band 4 (Red) and Band 5 (Near infrared) have been used for NDVI calculation (USGS, 2019). Eq. 1 is for calculating NDVI.

$$NDVI = \frac{Band\ 5 - Band\ 4}{Band\ 5 + Band\ 4} \quad (1)$$

2.4.2. Enhanced vegetation index

Enhanced vegetation index (EVI) is similar to NDVI and can be used to quantify vegetation greenness. However, EVI corrects some atmospheric conditions and canopy background noise and is more sensitive in areas with dense vegetation (USGS, 2021). Band 2 (Blue), Band 4 (Red) and Band 5 (Near-infrared) have been used for calculating EVI. Eq. 2 is for calculating EVI.

$$EVI = 2.5 \times \left(\frac{Band\ 5 - Band\ 4}{(Band\ 5 + 6) \times (Band\ 4 - 7.5) \times (Band\ 2 + 1)} \right) \quad (2)$$

2.5. Calculating land surface temperature (LST)

The method for calculating LST involves several steps. This method has been followed from Landsat 8 Data User Handbook from USGS (I. Vaughn, 2016). The first step is to convert the Thermal Infrared DN into Top of Atmosphere Radiance (TOR).

$$L_{\lambda} = ML \times QCAL + AL - O_i \quad (3)$$

Band 10 TIRS 1 (10.6–11.19 μm) 100 m of Landsat 8 has been used where L_{λ} is the TOR spectral radiance (Watts / ($\text{m}^2 \times \text{sr} \times \mu\text{m}$)). ML is the Radiance multiplicative band value. AL is the radiance add band value. $QCAL$ is a Quantized calibrated pixel value in DN. O_i is the correction value for Band 10, which is 0.29.

The second step is to convert the spectral radiance data into Top of Atmosphere (TOA) Brightness Temperature. The equation for this value is:

$$BT = \frac{K2}{\ln\left(\frac{K1}{L_{\lambda}} + 1\right)} - 273.15 \quad (4)$$

Here, BT is the top of atmosphere brightness temperature. L_{λ} is the TOR spectral radiance from Eq. (3). $K1$ is the $K1$ constant value,

and $K2$ is the $K2$ constant value of Band 10, which can be found in the metadata of the image set.

Land surface emissivity is the mean value of surface elements that has been calculated through NDVI. First, the Proportion of Vegetation (PV) has been calculated from Eq. (5).

$$PV = \left(\frac{NDVI - NDVI_{min}}{NDVI_{max} - NDVI_{min}} \right)^2 \quad (5)$$

Here, $NDVI$ has been found from Eq. (1). $NDVI_{min}$ and $NDVI_{max}$ is the minimum and maximum DN value of $NDVI$. After that, Eq. (6) has been used for Emissivity (E) calculation.

$$E = 0.004 \times PV + 0.986 \quad (6)$$

PV has been collected from Eq. (5), and 0.986 is the corresponding correction value.

In the last step, the LST has been calculated with values of BT and E from Eqs. (3) and (6).

$$LST = \frac{BT}{\left(1 + \left(\frac{\lambda BT}{c} \right) \times \ln(E) \right)} \quad (7)$$

Here, λ is the wavelength of emitted radiance. c is the velocity of light, h is Planck's constant, and s is Boltzman's constant.

2.6. Grid-based analysis

To identify the relationship between flood and vegetation, the total study area has been divided into 10,024 grids, each with 1 sq. km. After that, the flooded area and EVI have been calculated for each of these grids. Pearson correlation and simple linear regression has been done for these grids to find out the relationship between flooded areas and vegetation.

3. Results

3.1. Flood scenario

Table 1 shows the total amount of flooded areas from 2015 to 2020. The flood affects more regions in July than in August. The total area of flooded regions is decreasing from 2015 to 2018. But in 2019, it increased around 57% from the previous year, which is close to 2015. In 2020, the flooded areas didn't significantly decrease, unlike back in 2016 when it decreased around 17%.

A significant increase of flooded areas (62%) in August had happened only in 2017. Other than that, most of the year, the flood decreased in August. This result was expected in 2017, as Bangladesh faced a severe, long-lasting flood event (United Nations, 2017). Though in 2019, a massive rise in flooded area (120%) occurred in July, it didn't last long and eventually decreased around 15.02% in August. The first and second column of Fig. 2 illustrates the flood maps of all the years and months.

3.2. Vegetation change

The pixel wise total NDVI and EVI values from 2015 to 2020 has been shown in Table 2. The NDVI and EVI values are quite different from each other. The highest total NDVI value of the area was in 2016 but highest total EVI is in 2019. EVI is indicating the lowest value in 2016 which is the opposite of NDVI. The EVI value is indicating that from 2017, vegetaion is increasing each year in the area with an insignificant decrease (0.34%) in 2020. On the other hand, NDVI indicates the opposite, with a very little vegetation increase (1.35%) in 2018. Theoretically, EVI is more accurate than NDVI, but LST can be used to identify the accuracy as increased vegetation causes decreased temperature (Kafy et al., 2021a, 2021b; Kafy et al., 2020a). The third and fourth columns of Fig. 2 show the NDVI and EVI maps of the area, respectively.

Table 1
Total flooded area volume.

Year	Flooded area in July (Ha)	Percentage increase/decreased	Flooded area in August (Ha)	Percentage increase/decreased	Total flooded area (Ha)	Percentage increase/decreased
2015	172,200.60		230,825.62		403,026.22	
2016	229,102.34	+33.04%	103,315.88	-55.24	332,418.23	-17.52%
2017	161,146.89	-29.66%	167,448.60	+62.07	328,595.48	-1.15%
2018	131,380.72	-18.47%	115,501.55	-31.02	246,882.28	-24.87%
2019	290,182.64	+120.87%	98,157.78	-15.02	388,340.42	+57.30%
2020	245,021.77	-15.56%	104,140.29	+6.09	349,162.06	-10.09%

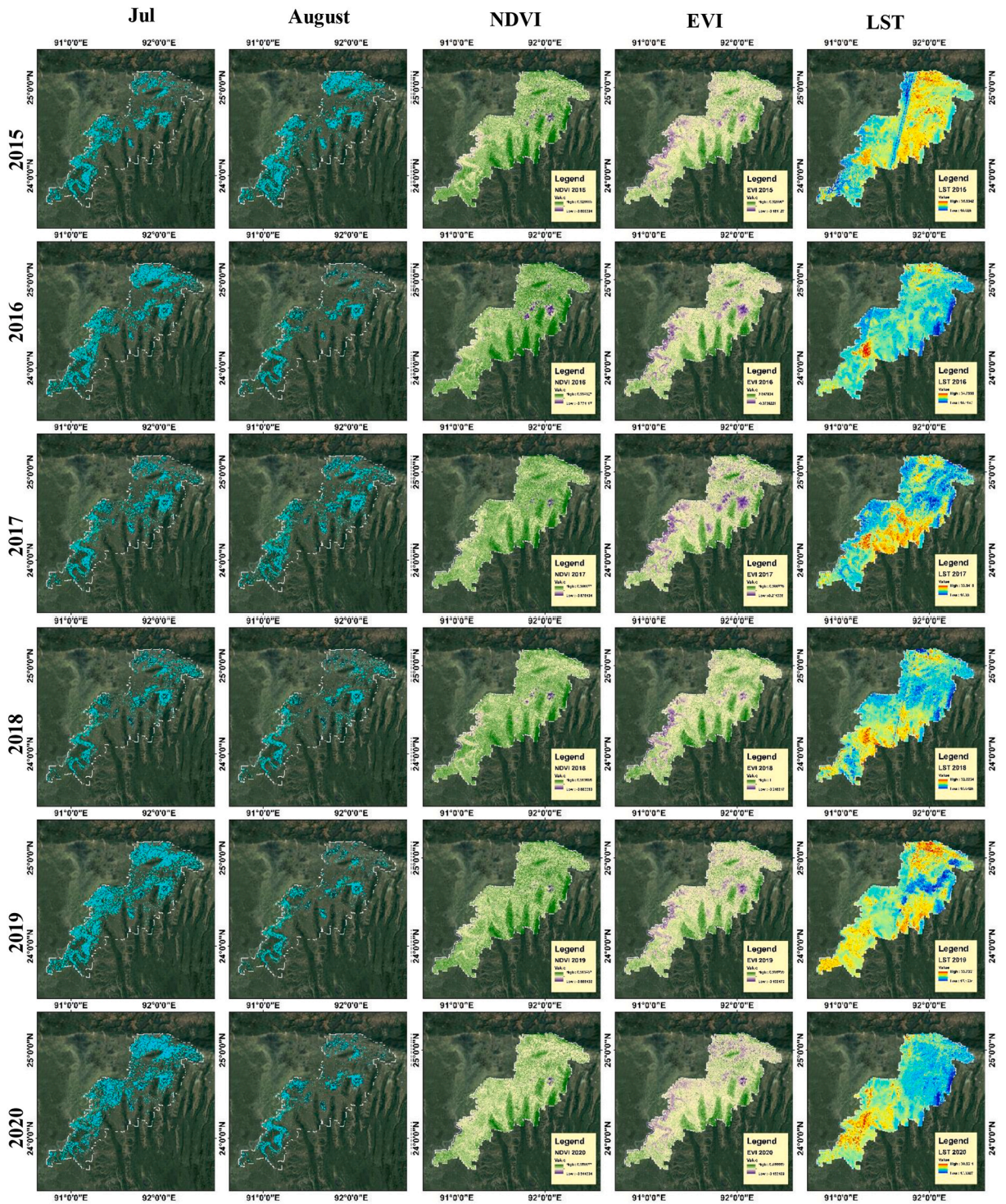


Fig. 2. Flood, NDVI, EVI and LST map of the study area.

3.3. LST dynamics

Table 3 shows the pixel-wise total LST values from 2015 to 2020. It reveals a continuous decrease of LST in each year except 2017. Major decrease can be seen in 2016 (6.03%) and 2020 (7.28%). The LST results are more compatible with EVI results than NDVI results. The basic assumption is that with the increase of vegetation, the temperature decreases, LST dynamics support the continuous

Table 2
Total NDVI and EVI.

Years	NDVI		EVI	
	Total NDVI values	Percentage increased/decreased	Total EVI values	Percentage increased/decreased
2015	6,819,906.04		4,619,609.719	
2016	7,019,984.734	+2.93%	4,473,961.996	-3.15%
2017	6,761,115.913	-3.69%	4,660,238.061	+4.16%
2018	6,852,079.754	+1.35%	4,901,437.186	+5.18%
2019	6,617,671.472	-3.42%	4,929,308.333	+0.57%
2020	6,387,083.242	-3.48%	4,912,709.181	-0.34%

Table 3
Total LST values.

Year	Total LST values	Percentage increased/decreased
2015	356,713,459.05	
2016	335,189,437.84	-6.03%
2017	342,737,560.76	+2.25%
2018	330,820,558.90	-3.48%
2019	327,516,354.51	-1.00%
2020	303,663,464.70	-7.28%

EVI changes. Fifth column of Fig. 2 shows the LST map of the area.

3.4. Relationship of flood with vegetation and LST

The change over the year for flooded areas, NDVI, EVI and LST has been shown in Fig. 3. Most of the year, the flooded area is decreasing with only a sudden rise in 2019. But after that, the flooded area decreased again in 2020. On the other hand, the EVI value increases, which indicates an opposite relationship with the flooded area. The EVI value started to increase in 2018 with the lowest volume of flooded areas. The Mean, Min and Max LST changes over time with a similar relation with flood and opposite relation with EVI. The LST is decreasing with an increase in EVI, which is expectable. Again, the NDVI values are not as authentic as the EVI. Overall results reveal that the vegetation increases with the decrease of the flooded area, and LST decreases.

3.5. Comparing flooded and non-flooded areas

The vegetation and LST dynamics in the flooded and non-flooded zone are shown in Table 4. It indicates a significant rise of mean EVI (21.19%) in 2018. In all the sample years, this year has the lowest volume of flooded areas. In 2019, the mean EVI raised again (11.25%) but not as much as the previous year. 2019 has the highest flood, and after that, in 2020, the mean EVI increase rate has fallen significantly from 11.25% to 2.04%. On the other hand, the mean EVI for the non-flooded area remains stable, with the highest increase in 2017 (5.38%). The increase rate continued through 2017 to 2019, with a slight decrease in 2020 (1.87%). Overall results suggest that the flood makes a noticeable impact on the vegetation dynamics. Also, the EVI decreases with extensive flooded areas.

The interrelation between LST and vegetation is also revealed. A continuous decrease of mean LST is observable from 2016 to 2020 for flooded regions and 2018 to 2020 for non-flooded regions. But in 2019, sudden LST increase (0.40%) in flooded areas and comparatively less LST decrease in non-flooded areas (1.31%) explains the high flood and low vegetation increase rate. Total scenario suggests that the fluctuation of flooded areas is impacting the vegetation growth and the LST dynamics. With the increase of flooded zones, the vegetation growth decreases, which is also responsible for an increase in mean LST.

3.6. Grid based correlation

The Pearson correlation value of the flooded area with NDVI and EVI is shown in Table 5. For all years studied, it was shown that the total flooded area had a negative connection with NDVI and EVI. The year with the highest negative correlation (-0.658) was 2017, when the country endured one of the longest floods in recent history. Another year with the largest total flooded areas in recent years is 2019 (-0.646). For all years, the EVI correlation value with the total flooded area is less than 0.56. The NDVI yields comparable findings. Because the NDVI value is not as exact as the EVI value, the readings are greater than the EVI value while still demonstrating a negative link between flooded areas and vegetation.

3.7. Grid-based linear regression analysis

The results of grid-based analysis from 2015 to 2020 is shown in Fig. 4. The X-axis is the flooded area, and the Y-axis is the total EVI value. The scatter plots reveal that the grids with high flooded area have a less total EVI value for each year. This statement is similar to

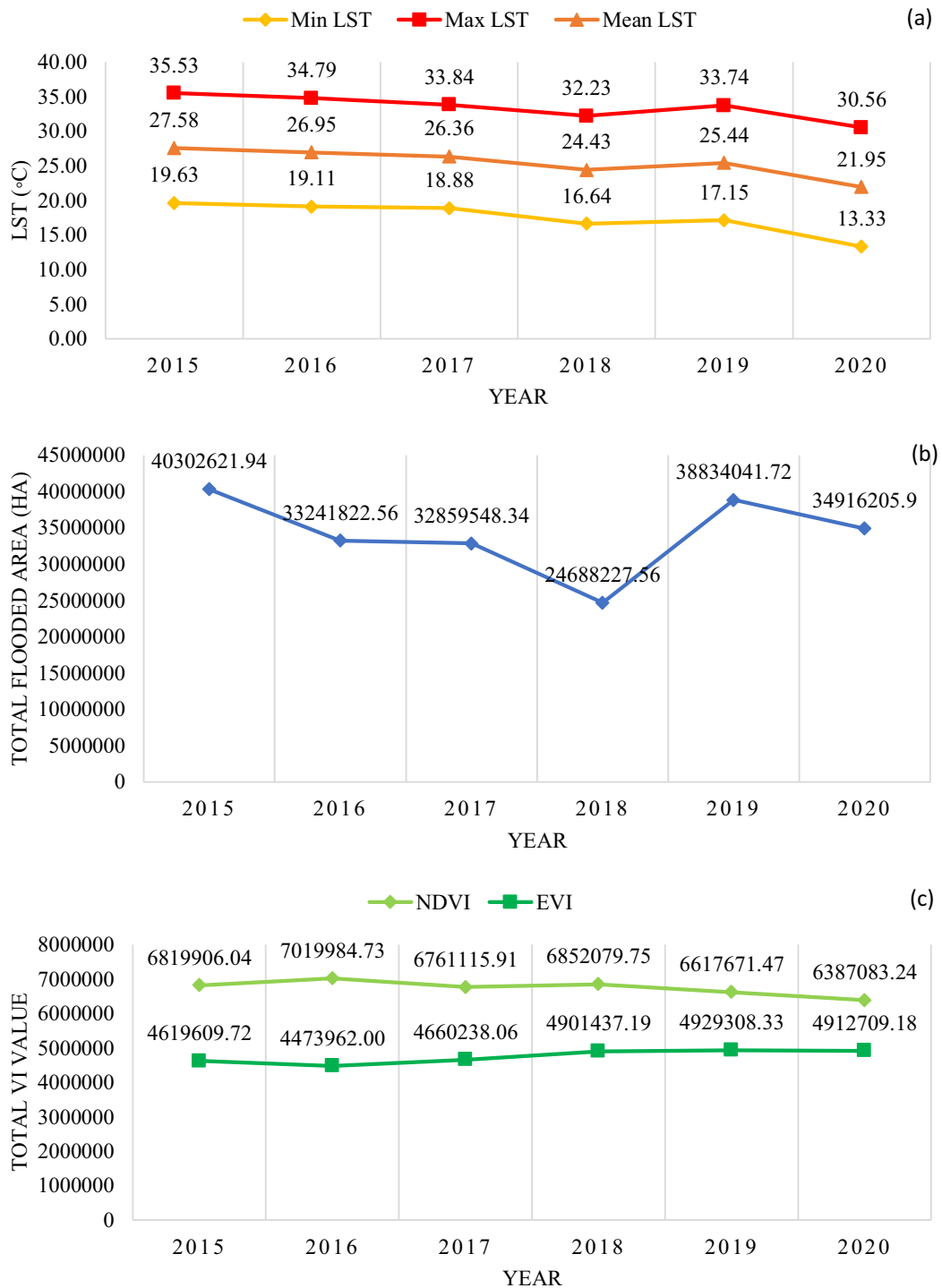


Fig. 3. Yearly ups and downs of (a) Mean, Minimum and Maximum LST (b) total flooded area, and (c)NDVI and EVI.

Table 4 which clearly indicates the negative relationship between flooded area and EVI. All the years have an R-squared value of more than 30%, which indicates the model's fitness. The highest R-squared value has been found for the year 2017, which is 43.25% (Fig. 4c). Also, the second-highest R-squared value is in the year 2019 with 41.60% (Fig. 4e). Flooded areas are significantly high in these years (Table 1), which is the main reason behind this negative impact on EVI. On the other hand, the lowest R-squared value is in 2018 (31.86%), when the flooded area was also the lowest (Table 1, Fig. 4d). This result also supports the negative relationship

Table 4
EVI and LST difference between flooded and non-flooded areas.

Flood year	Flooded area mean EVI	Increase/decrease	Non-flooded area mean EVI	Increase/decrease	Flooded area mean LST	Increase/decrease	Non-flooded area mean LST	Increase/decrease
2015	0.251		0.359		25.340		25.997	
2016	0.235	−6.71%	0.348	−3.19%	24.488	−3.36%	24.234	−6.78%
2017	0.205	−12.69%	0.367	+5.38%	24.374	−0.47%	24.935	+2.89%
2018	0.248	+21.19%	0.372	+1.49%	23.751	−2.55%	24.006	−3.73%
2019	0.276	+11.25%	0.386	+3.79%	23.847	+0.40%	23.691	−1.31%
2020	0.282	+2.04%	0.379	−1.87%	22.294	−6.51%	21.913	−7.50%

Table 5
Pearson correlation value of EVI and NDVI with total flooded area.

Year	EVI	NDVI
2015	−0.588	−0.461
2016	−0.632	−0.568
2017	−0.658	−0.33
2018	−0.564	−0.452
2019	−0.646	−0.439
2020	−0.595	−0.363

between flooded areas and vegetation.

4. Discussion

The GEE platform contains all accessible petabyte pictures from Sentinel-1 SAR and offers high-performance parallel computing equipment. It offers a pre-processing of Sentinel-1 data to the terrain level, decreasing the time required for intensive pre-processing of raw Sentinel-1 data. GEE offers chances to other scientists who do not have the technical expertise to deal with large-scale microwave data, supercomputers and cloud computing capabilities (Gorelick et al., 2017; Singha et al., 2020). Rapid flood response regions impacted are incredibly essential. A vast quantity of SAR data may be utilized over a wide area to identify areas inundated extremely rapidly (Singha et al., 2020). Therefore, this method may also be used in other areas of the globe, which makes it possible to monitor flood levels in close-to-real-time following additional testing in other places.

All the Sentinel-1 images available are helpful for large-scale quick flood mapping and monitoring in Bangladesh. In the flood maps produced by Sentinel-1, however, there are some uncertainties. The Sentinel-1 data is not available for June 2019 and 2020 on the study area, which is a crucial lack of this research. The ambiguity of flood maps may be due to Sentinel-1's limited time resolution of 6–12 days, depending on the location. As the floodwater varies quickly, it may not be enough to monitor the course of the flood. This is exacerbated in a vast region like Bangladesh, where precise identification of the high flood stages or maximum level has become a problem. Uncertainty occurs in the flood areas of SAR because of the environmental circumstances of the studied areas, such as the presence of winds in the collection of images, topography, kinds of vegetation and constructed areas. They may all have some effect on the outcome. Winds rage the surface of the water, disrupt the specular water reflection properties, and cause the flooded regions to be inaccurately defined. The radar shadow produced by the hilly landscape causes a surface water misclassification which may lead to an overestimation of regions inundated. The floodwater beneath vegetation cannot be identified using the C-band Sentinel-1 SAR, whereas L-band data like the PALSAR SAR may be used for flood mapping purposes under vegetation. Double bounce of radar signals from buildings hinders the detection of flooded regions inside metropolitan areas. However, the high-resolution SAR pictures have shown some promising results, and the impact of these variables has been insignificant. Flood regions may be inducing an underestimation or overestimation of the flood zone, depending on the selection of threshold values. Although the threshold values have been chosen based on the proposed and tried values, detecting all flooded sites may be limited. The selection of non-flooded SAR pictures may finally affect the identification of flooded regions. The seasonal changes in land cover and the variances in the acquisition settings for Sentinel-1 may lead to SAR signals at different times for water areas at the same place (Coverage, 2018; Rosenqvist et al., 2007; Singha et al., 2020). But currently, the combination of SAR and GEE is the best possible way to compute the effect of flood extensively.

5. Conclusion

This study considers the impact of flooding, a common natural calamity on the Indian subcontinent of the globe. The article demonstrates a definite negative association between total flooded area and vegetation, providing vital insights into flood's long-term effect. One of the key research bottlenecks is the inability to identify a direct association between flooded area and LST. Because LST has a very narrow value range, it is not feasible to present a statistical result with it. However, trend analysis (Fig. 3) reveals a definite association between LST and flood and vegetation, which is another significant finding from this study. Furthermore, it is a well-established epistemology that there is a definite negative association between LST and vegetation (Adeola Fashae et al., 2020; Fatemi and Narangifard, 2019; Kafy et al., 2021a, 2021b; Kafy et al., 2020b; Liu and Weng, 2009; Ullah et al., 2019). Also, the article

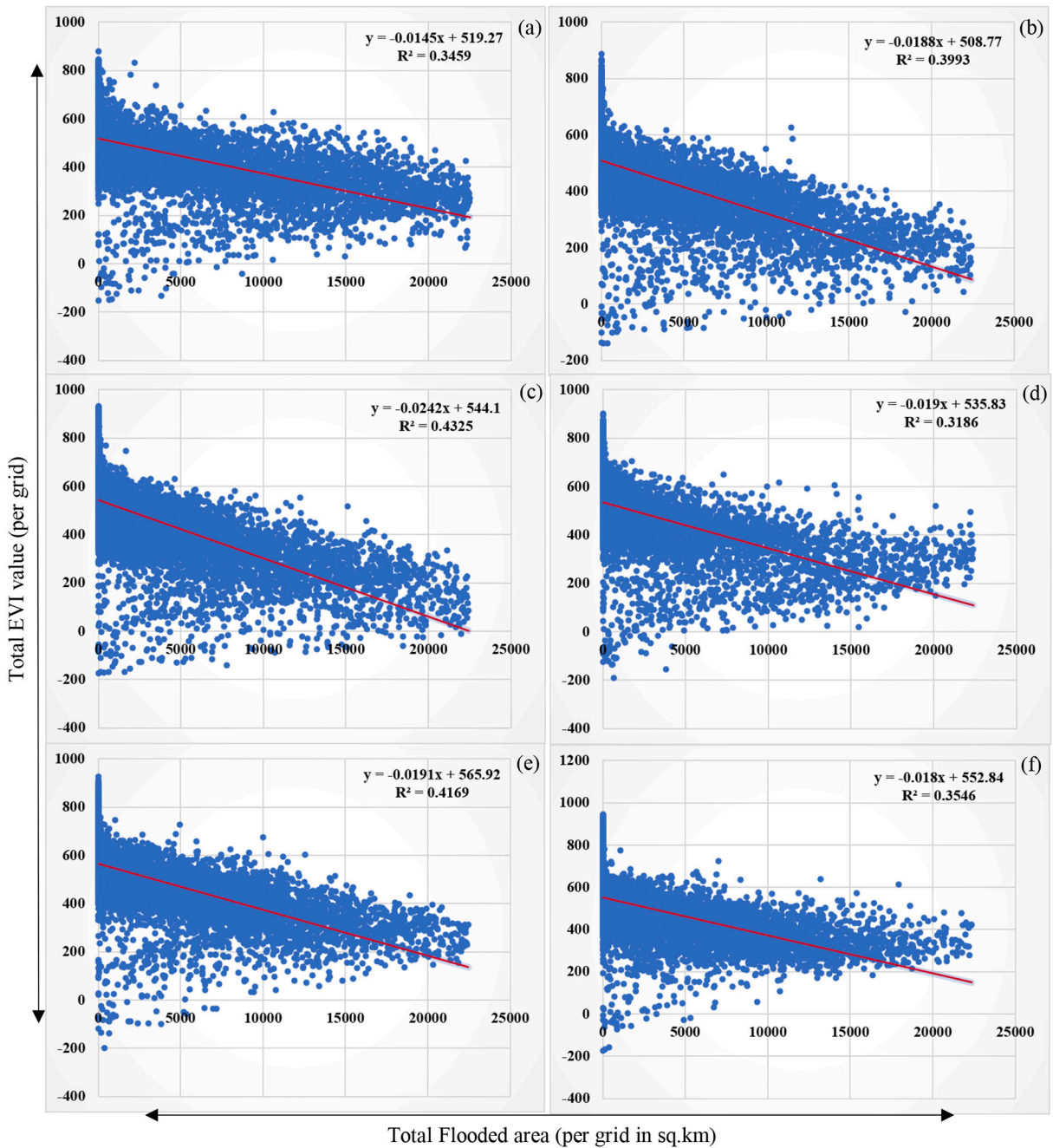


Fig. 4. Grid based analysis. The data from 10,024 grids of each year has been represented in scatter plot. X-axis is the flooded area and Y-axis is the total EVI value for each grid; (a) 2015; (b) 2016; (c) 2017; (d) 2018; (e) 2019; (f) 2020.

establishes a strong negative association between flooded areas and vegetation which indirectly establishes a positive relationship between flood and LST, as seen in Fig. 3's trend analysis.

Water catastrophes are a frequent occurrence in Bangladesh, and flooding is not a choice but a way of life. Floods of varied frequency and severity impact almost every place in Bangladesh. Bangladeshi floods may be associated with fluvial overflow, man-made water releases and/or severe rainfall and tides. The magnitude of the flood and the timing are a complicated mix of these events with extra precipitation in the upstream basin. Bangladesh's floods rely on total rainfall in the Ganges, Brahmaputra, and Meghna basins. Extreme floods occur when this river's peak water flow surpasses specific criteria. Every year flood in Bangladesh costs about \$2 billion in damage, mostly due to agricultural losses. With the changing climate in the future, the severity and frequency of floods are anticipated to rise, and the lowlands are increasingly in danger of severe flooding. Bangladesh is highly inhabited (more than 1000

people/km²), and there is continued private and public construction in low-lying regions, thus increasing damage and loss of life in severe floods. The long-term economic loss resulting from floods has hindered the government's development goals. The management of floods is a difficult job because of its inevitable nature, complexity and size. For Bangladesh, current structural and non-structural preventive measures are not adequate to reduce frequent flood occurrences. Local and national authorities must develop and implement adequate flood warning systems and spread flood information through contemporary communication technologies such as cell phones to reduce the impacts of floods. The government has to establish an effective flood management strategy and concentrate as a preventive measure to improve the local flood protection standard (Ali et al., 2019; Kuenzer et al., 2013; Singha et al., 2020).

As an agricultural economic-based country, this research derived a significant impact of flood in the context of Bangladesh. The research shows how much the flood affects the vegetation each year which is very crucial for the agricultural sustainability of the country. The temperature rises, which is an important factor of climate change, is also related to extensive floods. The research has created an opportunity to explore the deep climatic impact of a flood further. Most of the research related to floods mainly focuses on the devastating physical and infrastructural impact of the flood. But this research indicates a long-term climate change impact of flood, which can further extend and even contribute to the Urban Heat Island (UHI) effect study.

CRedit authorship contribution statement

Sk Nafiz Rahaman: Conceptualization, Methodology, Data curation, Formal analysis, Writing – original draft, Visualization, Software. **Nishat Shermin:** Conceptualization, Writing – review & editing.

Declaration of Competing Interest

The authors declare that they have no known competing financial interests or personal relationships that could have appeared to influence the work reported in this paper.

References

- Adeola Fashae, O., Gbenga Adagbasa, E., Oludapo Olusola, A., Oluseyi Obateru, R., 2020. Land use/land cover change and land surface temperature of Ibadan and environs, Nigeria. *Environ. Monit. Assess.* 192 <https://doi.org/10.1007/s10661-019-8054-3>.
- Ahmad, Q.K., Ahmed, A.U., 2003. Regional Cooperation in Flood Management in the Ganges-Brahmaputra-Meghna Region: Bangladesh Perspective, in: *Flood Problem and Management in South Asia*. Springer, Dordrecht, pp. 181–198. https://doi.org/10.1007/978-94-017-0137-2_9.
- Ali, M.H., Bhattacharya, B., Islam, A.K.M.S., Islam, G.M.T., Hossain, M.S., Khan, A.S., 2019. Challenges for flood risk management in flood-prone Sirajganj region of Bangladesh. *J. Flood Risk Manag.* 12 <https://doi.org/10.1111/jfr3.12450>.
- Amarnath, G., Rajah, A., 2016. An evaluation of flood inundation mapping from MODIS and ALOS satellites for Pakistan. *Geomatics Nat. Hazards Risk* 7, 1526–1537. <https://doi.org/10.1080/19475705.2015.1084953>.
- Amitrano, D., Di Martino, G., Iodice, A., Riccio, D., Ruello, G., 2018. Unsupervised rapid flood mapping using Sentinel-1 GRD SAR images. *IEEE Trans. Geosci. Remote Sens.* 56, 3290–3299. <https://doi.org/10.1109/TGRS.2018.2797536>.
- Banerjee, L., 2010. Effects of flood on agricultural productivity in Bangladesh. *Oxf. Dev. Stud.* 38, 339–356. <https://doi.org/10.1080/13600818.2010.505681>.
- Biswas, A.K., 2008. Management of Ganges-Brahmaputra-Meghna system: way forward. In: *Water Resources Development and Management*. Springer, Berlin, Heidelberg, pp. 143–164. https://doi.org/10.1007/978-3-540-74928-8_6.
- Brisco, B., Short, N., Van Der Sanden, J., Landry, R., Raymond, D., 2009. A semi-automated tool for surface water mapping with RADARSAT-1. *Can. J. Remote. Sens.* 35, 336–344. <https://doi.org/10.5589/m09-025>.
- Chowdhury, R.B., Moore, G.A., 2017. Floating agriculture: a potential cleaner production technique for climate change adaptation and sustainable community development in Bangladesh. *J. Clean. Prod.* 150, 371–389. <https://doi.org/10.1016/j.jclepro.2015.10.060>.
- Clement, M.A., Kilsby, C.G., Moore, P., 2018. Multi-temporal synthetic aperture radar flood mapping using change detection. *J. Flood Risk Manag.* 11, 152–168. <https://doi.org/10.1111/jfr3.12303>.
- Coverage, G., 2018. Geographical Coverage - Sentinel-1 - Sentinel Online - Sentinel [WWW Document]. URL. <https://sentinel.esa.int/web/sentinel/missions/sentinel-1/satellite-description/geographical-coverage> (accessed 8.24.21).
- Dasgupta, S., Huq, M., Khan, Z.H., Masud, M.S., Ahmed, M.M.Z., Mukherjee, N., Pandey, K., 2011. Climate proofing infrastructure in Bangladesh: the incremental cost of limiting future flood damage. *J. Environ. Dev.* 20, 167–190. <https://doi.org/10.1177/1070496511408401>.
- De Zan, F., Guarnieri, A.M., 2006. TOPSAR: terrain observation by progressive scans. *IEEE Trans. Geosci. Remote Sens.* 44, 2352–2360. <https://doi.org/10.1109/TGRS.2006.873853>.
- Doocy, S., Daniels, A., Packer, C., Dick, A., Kirsch, T.D., 2013. The human impact of earthquakes: a historical review of events 1980–2009 and systematic literature review. *PLoS Curr.* <https://doi.org/10.1371/currents.dis.67bd14fe457f1db0b5433a8ee20fb833>.
- ESA, 2021. User Guides - Sentinel-1 SAR - Interferometric Wide Swath - Sentinel Online - Sentinel [WWW Document]. URL. <https://sentinel.esa.int/web/sentinel/user-guides/sentinel-1-sar/acquisition-modes/interferometric-wide-swath> (accessed 8.11.21).
- ESA, E.S.A., 2019. Sentinel-1 SAR GRD: C-band Synthetic Aperture Radar Ground Range Detected, Log Scaling [WWW Document]. Earth Engine Data Cat. URL. https://developers.google.com/earth-engine/datasets/catalog/COPERNICUS_S1_GRD (accessed 8.10.21).
- ESA, E.S.A., 2020. WWF HydroSHEDS Void-Filled DEM, 3 Arc-Seconds [WWW Document]. URL. https://developers.google.com/earth-engine/datasets/catalog/WWF_HydroSHEDS_03VPDEM (accessed 8.10.21).
- Fatemi, M., Narangifard, M., 2019. Monitoring LULC changes and its impact on the LST and NDVI in district 1 of Shiraz City. *Arab. J. Geosci.* 12 <https://doi.org/10.1007/s12517-019-4259-6>.
- Gandhi, U., 2020. Flood Mapping - Part3 (Earth Engine Guided Project) - YouTube [WWW Document]. URL. https://www.youtube.com/watch?v=vYG31J-Hp7Q&ab_channel=SpatialThoughts (accessed 3.2.22).
- GEE, 2020. JRC Global Surface Water Mapping Layers, v1.2 [WWW Document]. Earth Engine Data Cat. URL. https://developers.google.com/earth-engine/datasets/catalog/JRC_GSW1_3_GlobalSurfaceWater (accessed 8.10.21).
- Google Earth Engine, 2021. USGS Landsat 8 Collection 1 Tier 1 Raw Scenes [WWW Document]. URL. https://developers.google.com/earth-engine/datasets/catalog/LANDSAT_LC08_C01_T1_RT (accessed 8.10.21).
- Gorelick, N., Hancher, M., Dixon, M., Ilyushchenko, S., Thau, D., Moore, R., 2017. Google Earth Engine: planetary-scale geospatial analysis for everyone. *Remote Sens. Environ.* 202, 18–27. <https://doi.org/10.1016/j.rse.2017.06.031>.
- Hostache, R., Chini, M., Giustarini, L., Neal, J., Kavetski, D., Wood, M., Corato, G., Pelich, R.M., Matgen, P., 2018. Near-real-time assimilation of SAR-derived flood maps for improving flood forecasts. *Water Resour. Res.* 54, 5516–5535. <https://doi.org/10.1029/2017WR022205>.

- Huang, C., Chen, Y., Wu, J., 2014. Mapping spatio-temporal flood inundation dynamics at large riverbasin scale using time-series flow data and MODIS imagery. *Int. J. Appl. Earth Obs. Geoinf.* 26, 350–362. <https://doi.org/10.1016/j.jag.2013.09.002>.
- IRRI, 2019. Bangladesh - Ricepedia [WWW Document]. URL. <https://ricepedia.org/bangladesh> (accessed 8.22.21).
- Islam, R., 2016. Bangladesh disaster-related statistics 2015. *Clim. Chang. Hum. Life Program.* 1–22.
- Jung, Y., Kim, Dongkyun, Kim, Dongwook, Kim, M., Lee, S.O., 2014. Simplified flood inundation mapping based on flood elevation-discharge rating curves using satellite images in gauged watersheds. *Water (Switzerland)* 6, 1280–1299. <https://doi.org/10.3390/w6051280>.
- Kafy, A., Rahman, M.S., Faisal, A., Hasan, M.M., Islam, M., 2020a. Modelling future land use land cover changes and their impacts on land surface temperatures in Rajshahi, Bangladesh. *Remote Sens. Appl. Soc. Environ.* 18, 100314 <https://doi.org/10.1016/j.rsase.2020.100314>.
- Kafy, A., Rahman, M.S., Faisal, A., Hasan, M.M., Islam, M., 2020b. Modelling future land use land cover changes and their impacts on land surface temperatures in Rajshahi, Bangladesh. *Remote Sens. Appl. Soc. Environ.* 18, 100314 <https://doi.org/10.1016/j.rsase.2020.100314>.
- Kafy, A., Faisal, A., Shuvo, R.M., Naim, M.N.H., Sikdar, M.S., Chowdhury, R.R., Islam, M.A., Sarker, M.H.S., Khan, M.H.H., Kona, M.A., 2021a. Remote sensing approach to simulate the land use/land cover and seasonal land surface temperature change using machine learning algorithms in a fastest-growing megacity of Bangladesh. *Remote Sens. Appl. Soc. Environ.* 21, 100463 <https://doi.org/10.1016/j.rsase.2020.100463>.
- Kafy, A., Rakib, A., Akter, K.S., Rahaman, Z.A., Faisal, A.-A., Mallik, S., Nasher, N.M.R., Hossain, M.I., Ali, M.Y., 2021b. Monitoring the effects of vegetation cover losses on land surface temperature dynamics using geospatial approach in Rajshahi city, Bangladesh. *Environ. Challenges* 4, 100187. <https://doi.org/10.1016/j.envc.2021.100187>.
- Kron, W., 2015. Flood disasters - a global perspective. *Water Policy* 17, 6–24. <https://doi.org/10.2166/wp.2015.001>.
- Kuenzer, C., Guo, H., Huth, J., Leinenkugel, P., Li, X., Dech, S., 2013. Flood mapping and flood dynamics of the mekong delta: ENVISAT-ASAR-WSM based time series analyses. *Remote Sens.* 5, 687–715. <https://doi.org/10.3390/rs5020687>.
- Kundzewicz, Z.W., Graczyk, D., Maurer, T., Pińskwar, I., Radziejewski, M., Svensson, C., Szwed, M., 2005. Trend detection in river flow series: 1. Annual maximum flow. *Hydrol. Sci. J.* 50, 797–810. <https://doi.org/10.1623/hysj.2005.50.5.797>.
- Kundzewicz, Z.W., Kanae, S., Seneviratne, S.I., Handmer, J., Nicholls, N., Peduzzi, P., Mechler, R., Bouwer, L.M., Arnell, N., Mach, K., Muir-Wood, R., Brakenridge, G. R., Kron, W., Benito, G., Honda, Y., Takahashi, K., Sherstyukov, B., 2014. Le risque d'inondation et les perspectives de changement climatique mondial et régional. *Hydrol. Sci. J.* 59, 1–28. <https://doi.org/10.1080/02626667.2013.857411>.
- Li, S., Sun, D., Goldberg, M.D., Sjöberg, B., Santek, D., Hoffman, J.P., DeWeese, M., Restrepo, P., Lindsey, S., Holloway, E., 2018. Automatic near real-time flood detection using Suomi-NPP/VIIRS data. *Remote Sens. Environ.* 204, 672–689. <https://doi.org/10.1016/j.rse.2017.09.032>.
- Lin, L., Di, L., Tang, J., Yu, E., Zhang, C., Rahman, M.S., Shrestha, R., Kang, L., 2019. Improvement and validation of NASA/MODIS NRT global flood mapping. *Remote Sens.* 11 <https://doi.org/10.3390/rs11020205>.
- Liu, H., Weng, Q., 2009. Scaling effect on the relationship between landscape pattern and land surface temperature: a case study of Indianapolis, United States. *Photogramm. Eng. Remote Sens.* 75, 291–304. <https://doi.org/10.14358/PERS.75.3.291>.
- Long, S., Fatoyinbo, T.E., Policelli, F., 2014. Flood extent mapping for Namibia using change detection and thresholding with SAR. *Environ. Res. Lett.* 9, 035002 <https://doi.org/10.1088/1748-9326/9/3/035002>.
- Manfreda, S., Di Leo, M., Sole, A., 2011. Detection of flood-prone areas using digital elevation models. *J. Hydrol. Eng.* 16, 781–790. [https://doi.org/10.1061/\(asce\)he.1943-5584.0000367](https://doi.org/10.1061/(asce)he.1943-5584.0000367).
- Martinis, S., Twele, A., Voigt, S., 2009. Towards operational near real-time flood detection using a split-based automatic thresholding procedure on high resolution TerraSAR-X data. *Nat. Hazards Earth Syst. Sci.* 9, 303–314. <https://doi.org/10.5194/nhess-9-303-2009>.
- Martinis, S., Kersten, J., Twele, A., 2015. A fully automated TerraSAR-X based flood service. *ISPRS J. Photogramm. Remote Sens.* 104, 203–212. <https://doi.org/10.1016/j.isprsjprs.2014.07.014>.
- Martinis, S., Plank, S., Ćwik, K., 2018. The use of Sentinel-1 time-series data to improve flood monitoring in arid areas. *Remote Sens.* 10, 583. <https://doi.org/10.3390/rs10040583>.
- Mason, D.C., Speck, R., Devereux, B., Schumann, G.J.P., Neal, J.C., Bates, P.D., 2010. Flood detection in urban areas using TerraSAR-X. *IEEE Trans. Geosci. Remote Sens.* 48, 882–894. <https://doi.org/10.1109/TGRS.2009.2029236>.
- Matgen, P., Hostache, R., Schumann, G., Pfister, L., Hoffmann, G., Savenije, H.H.G., 2011. Towards an automated SAR-based flood monitoring system: lessons learned from two case studies. *Phys. Chem. Earth* 36, 241–252. <https://doi.org/10.1016/j.pce.2010.12.009>.
- Mirza, M.M.Q., 2011. Climate change, flooding in South Asia and implications. *Reg. Environ. Chang.* 11, 95–107. <https://doi.org/10.1007/s10113-010-0184-7>.
- Monirul Qader Mirza, M., 2002. Global warming and changes in the probability of occurrence of floods in Bangladesh and implications. *Glob. Environ. Chang.* 12, 127–138. [https://doi.org/10.1016/S0959-3780\(02\)00002-X](https://doi.org/10.1016/S0959-3780(02)00002-X).
- Notti, D., Giordan, D., Caló, F., Pepe, A., Zucca, F., Galve, J.P., 2018. Potential and limitations of open satellite data for flood mapping. *Remote Sens.* 10, 1673. <https://doi.org/10.3390/rs10111673>.
- Panteras, G., Cervone, G., 2018. Enhancing the temporal resolution of satellite-based flood extent generation using crowdsourced data for disaster monitoring. *Int. J. Remote Sens.* 39, 1459–1474. <https://doi.org/10.1080/01431161.2017.1400193>.
- Pradhan, B., Hagemann, U., Shafapour Tehrani, M., Prechtel, N., 2014. An easy to use ArcMap based texture analysis program for extraction of flooded areas from TerraSAR-X satellite image. *Comput. Geosci.* 63, 34–43. <https://doi.org/10.1016/j.cageo.2013.10.011>.
- Qi, S., Brown, D.G., Tian, Q., Jiang, L., Zhao, T., Bergen, K.M., 2009. Inundation extent and flood frequency mapping using LANDSAT imagery and digital elevation models. *GIScience Remote Sens.* 46, 101–127. <https://doi.org/10.2747/1548-1603.46.1.101>.
- Rasid, H., Pramanik, M.A.H., 1993. Areal extent of the 1988 flood in Bangladesh: how much did the satellite imagery show? *Nat. Hazards* 8, 189–200. <https://doi.org/10.1007/BF00605441>.
- Rosenqvist, A., Shimada, M., Ito, N., Watanabe, M., 2007. ALOS PALSAR: a pathfinder mission for global-scale monitoring of the environment. *IEEE Trans. Geosci. Remote Sens.* 3307–3316. <https://doi.org/10.1109/TGRS.2007.901027>.
- Sanders, B.F., 2007. Evaluation of on-line DEMs for flood inundation modeling. *Adv. Water Resour.* 30, 1831–1843. <https://doi.org/10.1016/j.advwatres.2007.02.005>.
- Senthilnath, J., Shenoy, H.V., Rajendra, R., Omkar, S.N., Mani, V., Diwakar, P.G., 2013. Integration of speckle de-noising and image segmentation using synthetic aperture radar image for flood extent extraction. *J. Earth Syst. Sci.* 122, 559–572. <https://doi.org/10.1007/s12040-013-0305-z>.
- Shen, X., Wang, D., Mao, K., Anagnostou, E., Hong, Y., 2019. Inundation extent mapping by synthetic aperture radar: a review. *Remote Sens.* 11, 879. <https://doi.org/10.3390/rs11070879>.
- Sheng, Y., Gong, P., Xiao, Q., 2001. Quantitative dynamic flood monitoring with NOAA AVHRR. *Int. J. Remote Sens.* 22, 1709–1724. <https://doi.org/10.1080/01431160118481>.
- Singha, M., Dong, J., Zhang, G., Xiao, X., 2019. High resolution paddy rice maps in cloud-prone Bangladesh and Northeast India using Sentinel-1 data. *Sci. Data* 6, 1–10. <https://doi.org/10.1038/s41597-019-0036-3>.
- Singha, M., Dong, J., Sarmah, S., You, N., Zhou, Y., Zhang, G., Doughty, R., Xiao, X., 2020. Identifying floods and flood-affected paddy rice fields in Bangladesh based on Sentinel-1 imagery and Google Earth Engine. *ISPRS J. Photogramm. Remote Sens.* 166, 278–293. <https://doi.org/10.1016/j.isprsjprs.2020.06.011>.
- Taye, M.T., Ntegeka, V., Ogiraimo, N.P., Willems, P., 2011. Assessment of climate change impact on hydrological extremes in two source regions of the Nile River basin. *Hydrol. Earth Syst. Sci.* 15, 209–222. <https://doi.org/10.5194/hess-15-209-2011>.
- Tong, X., Luo, X., Liu, Shuguang, Xie, H., Chao, W., Liu, Shuang, Liu, Shijie, Makhinova, A.N., Makhinova, A.F., Jiang, Y., 2018. An approach for flood monitoring by the combined use of Landsat 8 optical imagery and COSMO-SkyMed radar imagery. *ISPRS J. Photogramm. Remote Sens.* 136, 144–153. <https://doi.org/10.1016/j.isprsjprs.2017.11.006>.
- Tsyganskaya, V., Martinis, S., Marzahn, P., Ludwig, R., 2018. SAR-based detection of flooded vegetation—a review of characteristics and approaches. *Int. J. Remote Sens.* <https://doi.org/10.1080/01431161.2017.1420938>.

- Twele, A., Cao, W., Plank, S., Martinis, S., 2016. Sentinel-1-based flood mapping: a fully automated processing chain. *Int. J. Remote Sens.* 37, 2990–3004. <https://doi.org/10.1080/01431161.2016.1192304>.
- Uddin, K., Matin, M.A., Meyer, F.J., 2019. Operational flood mapping using multi-temporal Sentinel-1 SAR images: a case study from Bangladesh. *Remote Sens.* 11 <https://doi.org/10.3390/rs11131581>.
- Ullah, S., Ahmad, K., Sajjad, R.U., Abbasi, A.M., Nazeer, A., Tahir, A.A., 2019. Analysis and simulation of land cover changes and their impacts on land surface temperature in a lower Himalayan region. *J. Environ. Manag.* 245, 348–357. <https://doi.org/10.1016/j.jenvman.2019.05.063>.
- United Nations, 2017. Bangladesh: Severe Floods in 2017 Affected Large Numbers of People and Caused Damage to the Agriculture Sector.
- UNU, 2019. UNU Update: Two Billion Face Flood Danger Soon [WWW Document]. URL. https://archive.unu.edu/update/archive/issue32_2.htm (accessed 8.22.21).
- USGS, 2019. Landsat Normalized Difference Vegetation Index [WWW Document]. URL. https://www.usgs.gov/land-resources/nli/landsat/landsat-normalized-difference-vegetation-index?qt-science_support_page_related_con=0#qt-science_support_page_related_con (accessed 8.13.21).
- USGS, 2021. Landsat Enhanced Vegetation Index [WWW Document]. U.S. Geol. Surv. URL. https://www.usgs.gov/core-science-systems/nli/landsat/landsat-enhanced-vegetation-index?qt-science_support_page_related_con=0#qt-science_support_page_related_con (accessed 8.13.21).
- Vaughn, L., 2016. Landsat 8 Data Users Handbook, vol. 8. Nasa, p. 97.